

# Behavior of CIII to CVI Emissions during the Recombining Phase of LHD Plasmas

Malay Bikas. CHOWDHURI, Shigeru MORITA<sup>1)</sup> and Motoshi GOTO<sup>1)</sup>

*Department of Fusion Science, Graduate University for Advanced Studies, Toki 509-5292, Gifu, Japan*

<sup>1)</sup>*National Institute for Fusion Science, Toki 509-5292, Gifu, Japan*

(Received 20 November 2007 / Accepted 28 February 2008)

Carbon emissions of CIII-CVI during the recombining phase of the Large Helical Device (LHD) plasma are studied to understand their behaviors. To achieve this, four resonance transitions of CIII ( $977 \text{ \AA}$ :  $2s^2 1S-2s2p^1P$ ), CIV ( $1548 \text{ \AA}$ :  $2s^2 S-2p^2P$ ), CV ( $40.27 \text{ \AA}$ :  $1s^2 1S-1s2p^1P$ ), and CVI ( $33.73 \text{ \AA}$ :  $1s^2 S-2p^2P$ ) are observed using absolutely calibrated VUV monochromators and EUV spectrometers. A one-dimensional impurity transport code has been used to calculate spectral emissivity under the consideration of measured  $n_e$  and  $T_e$  profiles. The temporal evolution of line emissions has been calculated and compared with the measured data. The comparison shows that the carbon density is 3% of the electron density. However, a discrepancy between the calculated and measured values has been noticed in CIII and CIV emissions. It has been argued that three-dimensional structures of CIII and CIV emissions are likely to be the reason for this difference, which is based on the presence of relatively high-density and high-temperature plasmas in edge ergodic layer in LHD. It is also found that the CV and CVI emissions during the recombining phase increase with electron density, whereas these are nearly constant during steady state phase. This strongly suggests the disappearance of the edge particle screening effect in the recombining phase.

© 2008 The Japan Society of Plasma Science and Nuclear Fusion Research

Keywords: impurity transport, carbon emission, recombining phase, screening effect, LHD

DOI: 10.1585/pfr.3.S1043

## 1. Introduction

For the study of impurity behavior in high-temperature plasmas, impurity densities in each charge state are usually analyzed using spectral absolute intensities measured from spectroscopic diagnostics in combination with a one-dimensional impurity transport code [1], which evaluates radial profiles of ion density and emissivity in all charge states on the basis of measured electron density and temperature profiles. In general, the impurity transport studies have been conducted during the steady state phase of discharges using either intrinsic or extrinsic impurity particles [2–5]. When the impurity time behavior is analyzed at a transient phase, especially the plasma termination phase, the duration is very short in the case of tokamaks because of the abrupt disruption after current termination. Even if the toroidal current is controlled for smooth termination of plasma, the magnetic field topology and resultant magnetic surface structure change rapidly as a function of time. On the other hand, in the stellarator cases, the magnetic field for confinement is supplied externally and is steady even during the transient phase of the discharges. The temporal evolution of impurity emissions from such plasmas can be easily computed under the presence of a steady magnetic surface.

In the Large Helical Device (LHD), the helical mag-

netic field for plasma confinement produced by superconducting magnetic coils enables steady state operation. It is therefore possible to analyze the transient period at initial and final phases of the discharges. Thus, the temporal behavior of edge carbon emissions is studied during the recombination phase of the LHD discharges through a comparison between the experimental and calculated radiated powers from different ionization stages of carbon.

It is well known that the enhancement of particle and energy transport by the stochastic magnetic field structure at the plasma edge, such as the ergodic layer in the LHD, should lead to a reduction of impurity content in the plasma [6]. During the recombining phase, the electron temperature decreases rapidly due to the absence of the heating source, and the plasma shrinks gradually inside the last closed flux surface (LCFS) before termination. Then, the role of the ergodic layer on edge impurity transport is likely to be different during the recombining and steady state phases of the discharges. In this context, carbon emissions from different ionization stages have been analyzed using electron density during the steady state and recombining phases of plasmas to examine the role of the ergodic layer on the behavior of edge carbon emissions.

author's e-mail: chowdhuri.malay@nifs.ac.jp

## 2. Experimental Setup

The experiment has been conducted with inwardly shifted configuration of  $R_{ax} = 3.6$  m and  $B_t = 2.75$  T. A discharge is initiated by electron cyclotron heating (ECH) and the plasma is sustained by three negative-ion-based neutral beam injection (NBI) devices. Several spectroscopic diagnostics covering visible to X-ray wavelength ranges have been installed to monitor and study the impurity behavior of LHD discharges. In the present study, emissions from different ionization stages of carbon have been measured using two extreme ultraviolet (EUV) spectrometers [7, 8] and two vacuum ultraviolet (VUV) monochromators [9]. Two absolutely calibrated EUV spectrometers cover 10-130 Å (EUV\_Short) and 50-500 Å (EUV\_Long) wavelength range. Back-illuminated VUV sensitive charge couple device (CCD) detectors are mounted with two EUV spectrometers and operated in full binning mode. Data from the CCD have been acquired every 5 ms. Four resonance transitions of CIII (977 Å,  $2s^2\ ^1S-2s2p\ ^1P$ ), CIV (1548 Å,  $2s\ ^2S-2p\ ^2P$ ), CV (40.27 Å,  $1s^2\ ^1S-1s2p\ ^1P$ ), and CVI (33.73 Å,  $1s\ ^2S-2p\ ^2P$ ) are monitored for this study. The CV and CVI emissions are measured using the EUV\_Short spectrometer with a spectral resolution of  $\sim 0.10$  Å at 40 Å. The resonance transitions from Li- (CIV) and Be-like (CIII) carbon ions are observed using two 20-cm normal incidence VUV monochromators equipped with electron multiplier tube detectors. The signal is acquired with a time interval of 100  $\mu$ s. The two VUV monochromators were absolutely calibrated using the carbon emissions, by comparing the raw signals with the absolutely calibrated EUV\_Long spectrometer for 50-500 Å. Two experimental intensity ratios of  $2s^2-2s3p$  (386.4 Å) to  $2s^2-2s2p$  (977 Å) transitions from CIII and of  $2s-3p$  (312.4 Å) to  $2s-2p$  (1548 Å) transitions from CIV were adopted for the calibration. Electron temperature and density profiles measured with Thomson diagnostics and line-integrated electron density measured with FIR diagnostics are used for the present analysis.

## 3. Description of Calculation

Analysis on temporal behaviors of carbon emissions in different ionization stages are based on the calculation of the line-integrated emissivity using a one-dimensional impurity transport code [1]. The time behavior of the impurity density profile is calculated using the following equation describing the ionization balance of an impurity ion:

$$\frac{\partial n_q}{\partial t} = -\frac{1}{r} \frac{\partial}{\partial r} (r\Gamma_q) + \alpha_{q-1} n_{q-1} n_e + \beta_{q+1} n_{q+1} n_e - (\alpha_q + \beta_q) n_q n_e, \quad (1)$$

where  $n_q$  and  $\Gamma_q$  are the ion density and particle flux of  $q$ th charge state, respectively. The parameters of  $\alpha$  and  $\beta$  represent the ionization and recombination rate coefficients, respectively. The empirical transport model [10], whose validity was confirmed in LHD, using the diffusion coefficient

$D$  and convective velocity  $V$  is given by

$$\Gamma_q = -D_q(r) \frac{\partial n_q}{\partial r} + V_q(r) n_q \quad (2)$$

$$\text{and} \quad V_q(r) = V(a) \frac{r}{a}. \quad (3)$$

Here,  $a$ ,  $D_q$ , and  $V_q$  are the plasma radius, diffusion coefficient, and convective velocity, respectively.

After the charge state calculation, the emissivity and brightness profiles of emission lines were evaluated. The emissivity of transition from level  $j$  to  $i$ ,  $\varepsilon(j, i)$ , is expressed by the relation of  $\varepsilon(j, i) = N_q(j)A(j, i)$ , where  $A(j, i)$  is the transition probability and  $N_q(j)$  is the density of the upper level  $j$  in charge state  $q$ . The emissivity is calculated from the level population in the upper level. The level population is generally determined by the collisional and radiative processes among several quantum levels [11]. However, the coronal model is assumed in the present case for simplicity. This assumption gives a good agreement with the C-R model calculation, at least, for the H- and He-like systems. Therefore, the relation can be written as  $\varepsilon(j, i) = N_q(j)A(j, i) = n_q n_e Q(i, j)$ , where  $Q(i, j)$  is the excitation rate coefficient for the transition from  $i$  to  $j$ . The excitation rate coefficient for individual lines was obtained from calculated results by Itikawa *et al.* [12].

## 4. Results and Discussions

### 4.1 Temporal evolution of carbon emissions during the recombining phase

A typical waveform of NBI discharge used in the present impurity study is shown in Fig. 1. The time evolution of carbon emissions has been analyzed at the recombining phase from 2.45 s to the end of plasma termination, where the electron temperature,  $T_e$ , decreases rapidly due to the absence of a heating source while  $n_e$  stays constant. The central electron temperature,  $T_e(0)$ , measured by Thomson scattering diagnostic was available until  $t = 2.62$  s. The CV and CVI emissions, on the other hand, dropped to zero at 2.628 s, and the CIII and CIV emissions disappeared 15 ms later because of their low ionization energies (I.E.) (CIII : 50 eV, CIV : 68 eV, CV : 392 eV, and CVI : 490 eV). Extrapolation of the measured  $T_e$  was therefore necessary to calculate the emissivity of the carbon emissions in different ionization stages.  $T_e$  was calculated from magnetic energy and line-averaged electron density  $\langle n_e \rangle$ . The measured and extrapolated  $T_e(0)$  and plasma radius  $r_b$  at the horizontally elongated plasma cross section are plotted in Fig. 2.  $T_e(0)$  and the plasma radius gradually decrease, and after  $t = 2.55$  s,  $T_e(0)$  begins to drop rapidly. The CIII and CIV emissions also start to increase rapidly at  $t = 2.55$  s.

Temporal evolution of carbon emissions during the recombining phase was calculated using a one-dimensional impurity transport code. The calculation was conducted on the averaged magnetic surface by replacing the elliptical shape of LHD plasmas with a circular shape. In this study,

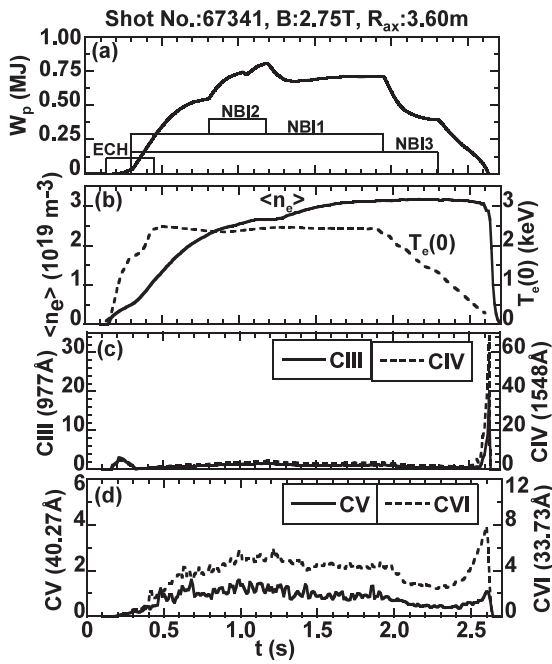


Fig. 1 Typical discharge for the present analysis; (a) plasma stored energy and NBI heating pulses, (b) line-averaged electron density (solid line) and central electron temperature (dashed line), (c) CIII (solid line) and CIV (dashed line) emissions, and (d) CV (solid line) and CVI (dashed line) emissions. All carbon emissions have unit of  $10^{14}$  photons  $\text{cm}^{-2}$   $\text{sr}^{-1}$   $\text{s}^{-1}$ . Data between  $t = 2.45$  and  $2.65$  s are used for analysis.

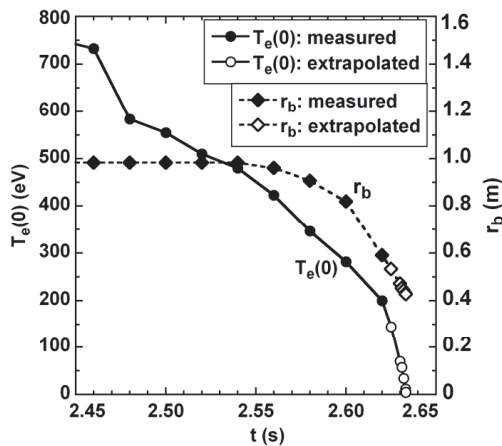


Fig. 2 Time behaviors of central electron temperature ( $T_e(0)$ : circles) and horizontal plasma radius ( $r_b$ : diamonds) at horizontally elongated plasma cross section during the recombining phase. Closed circles and diamonds indicate measured values, and open circles and diamonds indicate extrapolated values.

the diffusion coefficient  $D_q$  is considered independent of  $q$  and  $r$ , and the inward convection velocity  $V_q$  is considered a linear function of  $r$ . Here, the maximum value of  $V_q$  is given as  $V(a)$  at an average plasma radius,  $a$  (see Eq. 3). The values of  $D_q$  and  $V(a)$  are assumed to be  $0.2 \text{ m}^2 \text{ s}^{-1}$

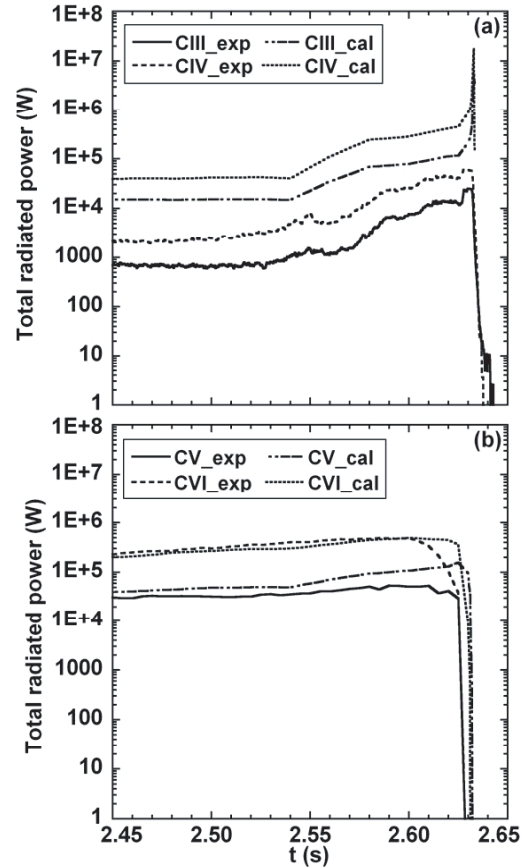


Fig. 3 Calculated and experimental total radiation power of (a) CIII and CIV and (b) CV and CVI. Solid (CIII and CV) and dashed (CIV and CVI) lines are experimental data. Dashed-dotted (CIII and CV) and dotted (CIV and CVI) lines indicate calculated data.

and  $1.0 \text{ ms}^{-1}$ , respectively.

Figure 3 illustrates the total radiation power emitted from Be-like CIII to H-like CVI, which are obtained by integrating the whole plasma surface of LHD. The experimental and calculated results are indicated with solid, dashed, dashed-dotted and dotted lines, respectively. In the calculation, the electron density is assumed to be 3% of the carbon density. All the carbon radiations increase gradually after turning off the heating power at  $t = 2.3$  s as  $T_e$  decreases. First, the CVI emissions reach the peak value at 2.60 s where  $T_e(0)$  is 280 eV. This is in good agreement with the calculation. Then, the CV and CVI radiations decrease rapidly and become zero at 2.625 s. At this moment,  $T_e(0)$  drops to less than 150 eV. The calculated values of CV and CVI radiations also drop at 2.630 s. Since the exposure time of the CCD detector is 5 ms in the present experiment, the difference between the measurement and calculation may originate from the uncertainty of the time window.

On the other hand, signal dynamic range of the CIII and CIV emissions is really large compared to the CV and CVI cases. The voltage applied to the secondary electron

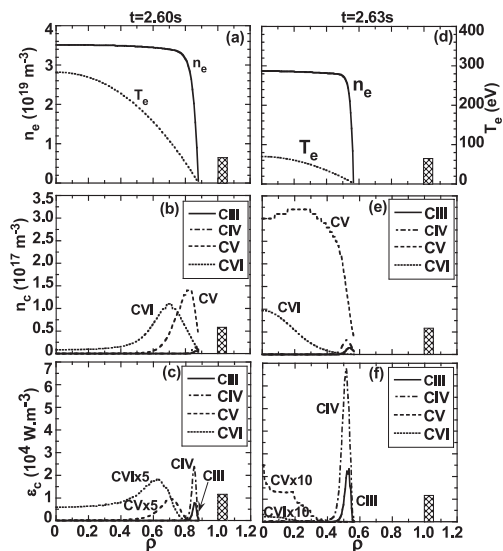


Fig. 4 Radial profiles of  $n_e$  and  $T_e$  ((a) and ((d)), densities ((b) and (e)) and emissivities ((c) and (f)) of CIII to CVI taken at two different time frames of 2.60 and 2.63 s, respectively. Horizontal axis means normalized radius,  $\rho$ . Hatched area indicates the ergodic layer outside the LCFS.

multiplier (SEM) is always adjusted to monitor the main discharges, not the plasma termination phase. Then, the signals of CIII and CIV are always saturated at the plasma termination phase, as seen during  $t = 2.628$ - $2.632$  s in the figure. The calculated values of CIII and CIV radiations reach the peak value at 2.632 s when  $T_e(0)$  becomes 12 eV. The calculation after 2.633 s is, however, practically impossible because of the extremely low electron temperature. In the discharge, very low temperature plasma is maintained until  $t = 2.645$  s, as seen in the CIII temporal behavior.

During the steady state phase of discharges, the carbon emissions are located primarily inside the narrow shell at the plasma edge. In LHD, the CIII and CIV emissions generally exist in the ergodic layer [13] surrounding the main plasma, and the CV and CVI emissions exist near the LCFS. During the recombining phase, the width of such emission shells is broadened as  $T_e$  decreases, and the shells move inside because of the reduction in the plasma size, as shown in Fig. 2. Calculated results on the radial profiles of carbon densities and emissivities are shown in Fig. 4. Figures 4 (a)-(c) and (d)-(f) are the radial profiles at  $t = 2.60$  and 2.63 s in Fig. 3, respectively. The position of the ergodic layer is shown by a hatched area outside the LCFS ( $\rho = 1$ ). It can be seen from the figure that the emission shells of CIII to CVI move inside the LCFS at these times, since the plasma size is reduced. The CVI emission reaches the maximum value at 2.60 s, and the CV and CVI emissions disappear entirely at 2.63 s. Figures 4(a) and (c) are the measured  $n_e$  and  $T_e$  profiles, respectively, used in the calculation. The CIII and CIV emissions are always located at

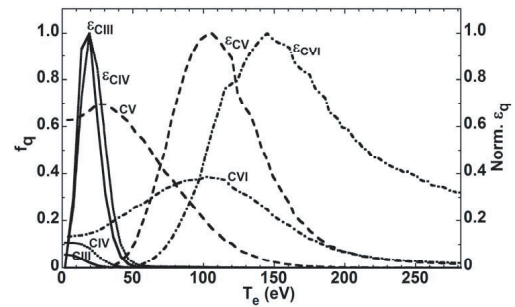


Fig. 5 Fractional abundance ( $f_q$ ) and emissivity (Norm.  $\epsilon_q$ ) plotted with  $T_e$  for CIII (solid line), CIV (dotted line), CV (dashed line), and CVI (dashed-dotted line) at  $t = 2.60$  s. Notations of CIII to CVI and  $\epsilon^{\text{CIII}}$  to  $\epsilon^{\text{CVI}}$  indicate fractional abundance and emissivity of each charge state, respectively. Emissivity is normalized by its peak value.

the plasma edge in these time frames and have sharp peaks.

On the other hand, the CV and CVI emission profiles are quite different. At  $t = 2.60$  s, the shell widths of the CV and CVI densities become wider (see Fig. 4(b)), and resultant emission profiles also become much wider (see Fig. 4(c)). In particular, the tendency of the CVI emission profile is remarkable, because the excitation rate coefficient of CVI emission drops rapidly at  $T_e < 200$  eV. This effect can be seen in the difference between the peak positions of CVI density profile ( $\rho = 0.67$  in Fig. 4(b)) and emissivity profile ( $\rho = 0.63$  in Fig. 4(c)).

Figure 5 shows the fractional abundances and emissivities for CIII to CVI emissions at  $t = 2.60$  s. In the figure, the horizontal axis in Fig. 4(b) and (c) is replaced by  $T_e$ . Here, the emissivity of individual charge states is normalized to their peak value. It can be seen that the peak of the CVI density profile occurs at  $T_e = 105$  eV ( $\rho = 0.67$ ) while the peak of the emissivity profile,  $\epsilon^{\text{CVI}}$ , appears at  $T_e = 150$  eV ( $\rho = 0.63$ ). At  $t = 2.63$  s, the CV and CVI emissions disappear completely, as seen in Fig. 4(f), whereas the CV and CVI densities increase at the plasma center (see Fig. 4(e)). The excitation rate coefficient of CVI shown in Fig. 4 (f) ( $1.97 \times 10^{-18} \text{ m}^3 \text{ s}^{-1}$  at  $T_e(0) = 70$  eV) is 33 times smaller than that in Fig. 4(c) ( $6.69 \times 10^{-17} \text{ m}^3 \text{ s}^{-1}$  at  $T_e(0) = 280$  eV).

The calculation of the total radiation power for the CV and CVI emissions shows good agreement with the experiment, for evaluation of 3% carbon density. However, the CIII and CIV results are ten times larger than the experimental values. The reason for this is not clear at present. At least, it is known that the emission distribution from low ionized ions and neutral atoms is toroidally and poloidally inhomogeneous because of the presence of the ergodic layer. Indeed, recent studies indicate that the emissions from CIII and CIV have asymmetric features reflecting the field line structure of the ergodic layer. In particular, the vertical profile of CIV exhibits four peaks, which

are formed at the inboard side near the X-point, in addition to the top and bottom edge peaks at the horizontally elongated plasma cross section [14]. It is reported that particle recycling is enhanced at the inboard side [15]. It is also observed that the inhomogeneous poloidal distribution of the neutral emissions arises mainly from the inhomogeneity in the neutral particle density, not from the nonuniformity of the electron temperature and density [16]. This is likely to be one of the reasons for the difference.

## 4.2 Density dependence of carbon emissions during the recombining and steady state phases

Finally, the CVI emission is examined for several discharges at the peak value during the recombining phase, where the plasma begins to shrink and the size becomes a little smaller than the LCFS. The CVI emission during the steady-state phase is also studied for comparison. Intensities of the CVI emission are plotted against  $\langle n_e \rangle$ , as shown in Fig. 6(a) and (b) for the recombining and steady state phases, respectively. CVI emission intensities normalized to the density and excitation rate coefficient ( $\text{CVI}/(n_e Q)$ ), which means the CVI density, are also plotted in the figure. The excitation rate coefficient is calculated at the electron temperature at the LCFS for the steady state phase and at the central electron temperature for the recombining phase.

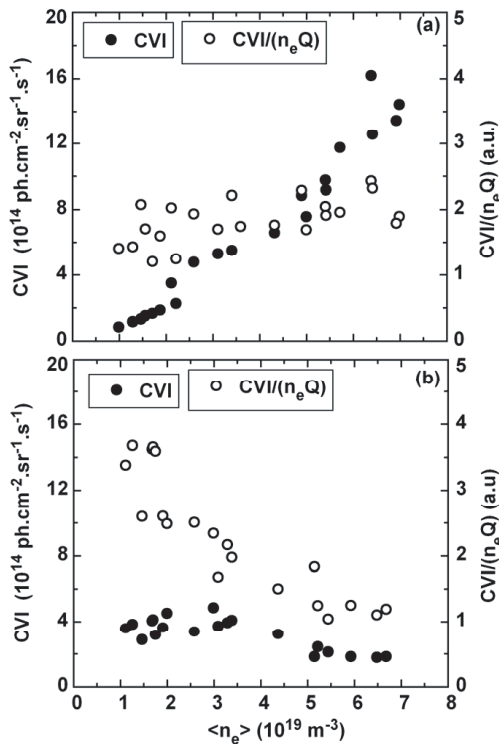


Fig. 6 CVI intensity (closed circles) and  $\text{CVI}/(n_e Q)$  (open circles) plotted against line-averaged electron density  $\langle n_e \rangle$  for the (a) recombining and (b) steady state phases. Value of  $Q$  indicates excitation rate coefficient of CVI.

This choice is reasonably correct since the CVI emission location is estimated from the CV radial profile. The difference between the two phases is very clear. The CVI emission intensities from the recombining phase increase with  $\langle n_e \rangle$ , whereas those from the steady state phase decrease with  $\langle n_e \rangle$ . Thus, we find a clear difference in the carbon density behavior with  $\langle n_e \rangle$ . In other words, the CVI density is nearly constant with  $\langle n_e \rangle$  for the recombining phase, but it definitely decreases with  $\langle n_e \rangle$  for the steady state phase.

CV emissions and densities also follow a trend similar to that of CVI, as shown in Figs. 7(a) and (b) for the recombining and steady state phases, respectively. The CV emission intensities increase with  $\langle n_e \rangle$  during the recombining phase while it is nearly constant during the steady state phase. On the other hand, the CIII emission intensities, which suggest the carbon influx for the ionizing plasma during the steady state phase, increase with  $\langle n_e \rangle$  for both phases, as shown in Fig. 8. The CIII emission intensities for the recombining phase are saturated at densities greater than  $5 \times 10^{19} \text{ m}^{-3}$ . The intensities of CIV emission also show the same tendency as depicted in Fig. 9 and are saturated at densities greater than  $3.5 \times 10^{19} \text{ m}^{-3}$ . The reduction of the CV and CVI densities for the steady state phase may suggest the impurity screening effect. Increasing the density in the ergodic layer causes an increase in the friction force, which leads to impurity screening. The

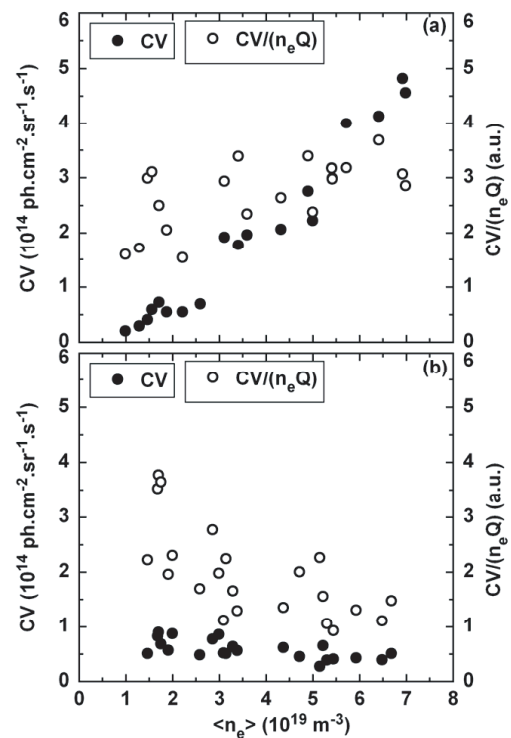


Fig. 7 CV intensity (closed circles) and  $\text{CV}/(n_e Q)$  (open circles) plotted against line-averaged electron density  $\langle n_e \rangle$  for the (a) recombining and (b) steady state phases. Value of  $Q$  indicates excitation rate coefficient of CV.

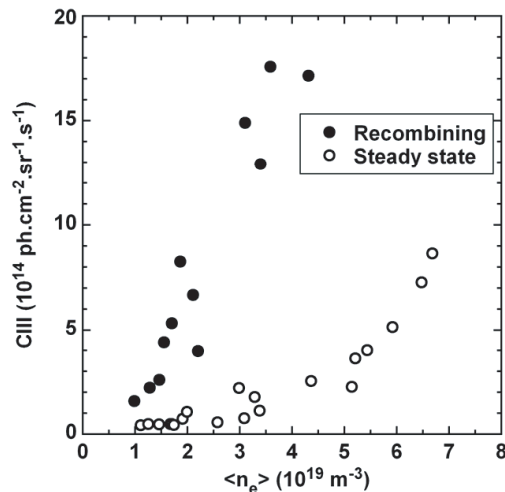


Fig. 8 CIII intensity against line-averaged electron density  $\langle n_e \rangle$  for the recombining (closed circles) and steady state phases (open circles).

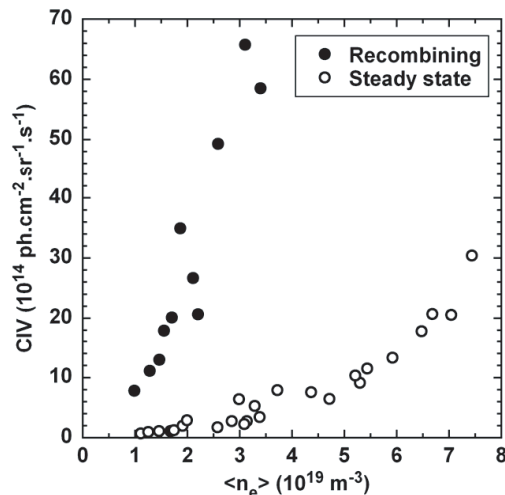


Fig. 9 CIV intensity against line-averaged electron density  $\langle n_e \rangle$  for the recombining (closed circles) and steady state phases (open circles).

carbon emissions in case of the recombining phase are not easy to understand, because the CIII emissions do not indicate simply the influx. In addition, the origin of the carbon source is very unclear since the plasma shrinks and is completely detached from the divertor plates and vacuum wall. Further investigation of carbon behavior during the recombining phase is needed.

## 5. Summary

Temporal evolution of carbon emissions during the recombining phase of the discharges was studied through the

calculation of spectral emissivity using a one-dimensional transport code. The calculation of CV and CVI emissions indicate that the carbon density is 3 % of the electron density. The difference between density and emission locations as a function of  $T_e$  was studied for CV and CVI emissions. The discrepancy between computed and experimental CIII and CIV emissions was found. Although the reason behind this is not completely clear, it is argued that the three-dimensional structure of CIII and CIV emissions might be responsible for the differences.

Comparison of CV and CVI emissions during the steady state and recombining phases reveal the difference in their dependence on  $n_e$ . Both intensities increase with  $n_e$  during the recombining phase but remain nearly constant during the steady state phase. On the other hand, the CIII and CIV emission intensities increase with  $n_e$  in both the phases. From this observation, it is suggested that impurity screening effect is enhanced with  $n_e$  during the steady state phase and it disappears during the recombining phase.

## Acknowledgments

The authors would like to thank the members of the LHD experimental group for their technical support. This work was carried out partly under the LHD project financial support (NIFS06ULPP527). This work was also partly supported by the JSPS-CAS Core-University Program in the field of “Plasma and Nuclear Fusion.”

- [1] T. Amano, J. Mizuno and T. Kako, Int. Rep. IIPJ-616, Institute for Plasma Physics, Nagoya University (1982).
- [2] J.C. Moreno and E.S. Marmor, Phys. Rev. A **31**, 3291 (1985).
- [3] H. Chen *et al.*, Plasma Phys. Control. Fusion **43**, 1 (2001).
- [4] H. Nozato, S. Morita, M. Goto *et al.*, Phys. Plasmas **11**, 1920 (2004).
- [5] R. Burhenn *et al.*, Fusion Sci. Technol. **46**, 115 (2004).
- [6] Ph Ghendrih *et al.*, Plasma Phys. Control. Fusion. **44**, 1653 (1996).
- [7] M.B. Chowdhuri, S. Morita and M. Goto, Appl. Opt. **47**, 135, (2008).
- [8] M.B. Chowdhuri, S. Morita, M. Goto *et al.*, Rev. Sci. Instrum. **78**, 023501 (2007).
- [9] S. Morita, M. Goto *et al.*, Physica Script **T91**, 48 (2001).
- [10] S. Morita, M. Goto *et al.*, Plasma Sci. Technol. **8**, 55 (2006).
- [11] M. Goto, J. Quant. Spect. Rad. Trans. **76**, 331 (2003).
- [12] Y. Itikawa *et al.*, Atomic Data and Nuclear Data Tables **33**, 149 (1985).
- [13] S. Morita, T. Morisaki, M. Goto *et al.*, Nucl. Fusion **47**, 1033 (2007).
- [14] R. Katai, S. Morita and M. Goto, Rev. Sci. Instrum. **77**, 10F307 (2006).
- [15] M. Goto and S. Morita, Phys. Rev. E **65**, 026401 (2002).
- [16] H. Yamazaki, M. Goto, S. Morita *et al.*, Plasma Fusion Res. **2**, S1000 (2007).